Nature Communications

https://doi.org/10.1038/s41467-026-70260-2

Article in Press

A Soft-Robotic Biomimetic Benchtop Model for Esophageal Motility Simulation

Received: 20 June 2025

Accepted: 17 February 2026

Cite this article as: Kilroy, S., Patankar, N.A., Chan, W.W. *et al.* A Soft-Robotic Biomimetic Benchtop Model for Esophageal Motility Simulation. *Nat Commun* (2026). https://doi.org/10.1038/s41467-026-70260-2

Seán Kilroy, Neelesh A. Patankar, Walter W. Chan, Giovanni Traverso & Eoin D. O'Cearbhaill

Title

A Soft-Robotic Biomimetic Benchtop Model for Esophageal Motility Simulation.

Author List

S. Kilroy,[1,2] N.A. Patankar,[3] W.W. Chan,[2] G. Traverso, [2,4,5,6]* E.D. O'Cearbhaill[1]*

Affiliations

[1]School of Mechanical & Materials Engineering, UCD Centre for Biomedical Engineering, UCD Conway Institute, University College Dublin; Dublin, Ireland.
[2]Division of Gastroenterology, Hepatology and Endoscopy, Brigham and Women's Hospital, Harvard Medical School; Boston, USA.
[3]Department of Mechanical Engineering, McCormick School of Engineering; Northwestern University, Evanston, Illinois, USA.
[4]Department of Mechanical Engineering, Massachusetts Institute of Technology; Boston, MA, USA
[5]Koch Institute for Integrative Cancer Research, Massachusetts Institute of Technology; Boston, USA.
[6]Broad Institute of MIT and Harvard, Cambridge, MA, USA.

*Corresponding authors. Email: cgt20@mit.edu and eoin.ocearbhaill@ucd.ie.

Abstract

Large animal models, while valuable, are expensive, time-consuming, and limited to discrete interventional or terminal timepoints, while existing benchtop models do not offer an accurate representation of the esophageal environment. Moreover, current pre-clinical models cannot effectively simulate swallowing dysfunction (dysphagia), restricting progress in understanding motility disorders like achalasia and hindering evidence-based dietary recommendations. In response, we present RoboGullet, a biomimetic soft-robotic model with independent localized longitudinal and circumferential muscle actuation enabling, for the first time, simulation of both normal and diseased esophageal motility. We further enhance realism with a biohybrid variant, RoboGullet+, incorporating porcine esophageal mucosa/submucosa. We demonstrate this platform's versatility through three key applications: assessing stent migration, simulating achalasia I-III within clinical diagnostic criteria, and analyzing bolus swallowing. Our findings reveal that: (1) stent migration increases over fivefold when incorporating longitudinal muscle movement versus isolated circumferential; (2) using a viscous non-Newtonian bolus improves high-resolution manometry diagnostic sensitivity of Achalasia III through increasing the Distal Latency diagnostic metric by 20.83%; and (3) stirring Greek-style yoghurt (common non-Newtonian dietary recommendation) significantly improves bolus transit versus unstirred for Achalasia Types I-II patients. This establishes RoboGullet+ as a powerful translational tool, advancing our understanding of esophageal motility and its therapeutic interventions.

Introduction

The esophagus's primary function is to facilitate swallowing, the transportation of bolus from mouth to stomach [1]. This is achieved through the coordinated peristalsis of two muscular layers (an inner circumferential and an outer longitudinal layer) and deglutitive relaxation of an Upper Esophageal Sphincter (UES) and a Lower Esophageal Sphincter (LES) which respectively control intake and outflow [2]. Dysphagia, or difficulty swallowing, affects about 20% of the global population and up to 50% of people over the age of 60 [3]. This can be for a number of reasons, such as malignancy and motility disorders such as achalasia [4]. Approximately 35% of dysphagia cases are malignant [5], primarily resulting from esophageal cancer [6] where tumors partially or completely obstruct the esophageal lumen. Approximately 5% of cases are due to achalasia [5], a major motility disorder characterized by incomplete LES relaxation during swallows combined with an absence of peristalsis [4].

The majority of malignant dysphagia cases are incurable at diagnosis [6]. These patients require palliative treatment, most commonly through esophageal self-expanding metal stents (SEMS) due to their ease of placement, availability, clinical effectiveness, and potential for removal if necessary [6]. SEMS include uncovered (U-SEMs), partially-covered (PC), and fully-covered (FC) types. However, these designs have limitations: tissue ingrowth in PC and U-SEMs can re-block the channel and render them unremovable [7]. Conversely, the lack of tissue ingrowth in FC SEMS results in high migration rates (29–40% [8]). Treatment of achalasia, like malignancy, is generally palliative and primarily targets relaxing the LES to relieve the outflow obstruction. It, however, has excellent results, seeing >90% success with surgery [9]. Notwithstanding, dietary modification is also often suggested, particularly for patients who failed therapy or those who are poor surgical candidates for definitive interventions. Despite this, there has been limited research into evidence-based diet recommendations [10]. Achalasia diagnosis is extensively described in the literature, with the gold standard being high resolution manometry (HRM) [11,12]. As a chronic, progressive disease, early manometric changes, especially in type III achalasia, may not fulfil established diagnostic criteria and are often misdiagnosed or missed entirely. It has been suggested that altering the bolus viscosity used for test swallows during HRM can accentuate diagnostic yield [13,14].

Current *in vivo* evaluations of dysphagia remain limited to, large animal models for malignant dysphagia or limited clinical studies for achalasia [15]. These studies can be expensive and time-consuming, provide information only at specific interventional and terminal timepoints, and lack repeatability across samples. This poses challenges for functional device assessments and for standardized dietary recommendations. Benchtop models are used as alternatives or supplements to pre-clinical *in vivo* models for device testing, disease evaluation, and surgical training. Highly accurate biomimetic benchtop models exist for some aspects of the body, such as the heart [16]. However, replication of key physical and functional properties in esophageal or gastrointestinal (GI) tract models has been limited. Rigid roller systems, the most basic approach [17], simulate peristaltic waves mechanically. Soft models better replicate the organ's conformable nature [18]. Here, soft expandable pressure vessels [19], cables [20], and pneumatic cuffs [21], pistons [22], and chambers [23,24] have been employed, with these pneumatic artificial muscles (PAMs) creating the necessary radial contractile movement. These models, however, lack realistic tissue interaction and only simulate circumferential muscles. This neglects the longitudinal muscles, which provide axial movement and account for half the musculature involved in

GI motility [25]. Peerlink et al. [26] did introduce an intestinal model with longitudinal movement but it is without independent PAMs and thus control. Although PAMs for axial movement exist [27–29], no GI motility model has yet integrated them with radial PAMs. This is due to the challenges in fabricating two concentric layers with differing independently actuating directions – typically PAMs achieve singular direction/shape control with a single soft material and an embedded, less extensible layer [30]. Crucially, this lack of independent circumferential and longitudinal muscle control, on top of not fully describing normal esophageal motility, means motility disorders, where the muscle layer's contractions may be asynchronous or vary in amplitude, cannot be simulated

Here we propose RoboGullet+, a soft-robotic biomimetic benchtop model of the esophagus, which offers controlled replication of esophageal motility mechanics. Additionally, it facilitates the creation of bio-hybrid structures to further match the frictional properties and compliance of native esophagus. We demonstrate that this model can recreate normal and diseased esophageal motility accurately. Furthermore, we demonstrate the versatility of the model by evaluating commercial stent migration and the effects that bolus properties have on achalasia diagnosis and swallowing, showing that the model can be used to simulate a multitude of conditions relevant to device evaluation, disease management, and personalized clinical testing.

Results

Study design and workflow

In this work, we propose a biomimetic soft-robotic model that replicates the movement of circumferential and longitudinal muscles to accurately simulate esophageal motility (Supplementary Movie 1). The design process is illustrated in Fig. 1a. The esophagus comprises concentric layers of circumferential (inner) and longitudinal (outer) muscles that locally contract and relax to achieve radial and axial movement respectively. This independence allows pathophysiological simulation where muscles are asynchronous [31–34]. Similar to Park et al. [29], we used a biomimetic approach to design the soft-robotic representation of the muscle orientation and position (Fig. 1a). This consists of two concentric layers of pneumatically actuated hexagonal rings. The inner layer, fabricated from a softer silicone (EcoFlex 00-30, SmoothOn), mimics the circumferential muscles while the outer layer, made of a stiffer silicone (DragonSkin 20), constrains radial expansion and mimics the longitudinal muscle movement via a bellows-type PAM design (Supplementary Fig. 1) [35]. Similar to other GI motility models [23,26] and the peristaltic earthworm body [36], the model consists of repeating segments of concentric rings. Fabrication involved a dual-material lost-wax casting procedure (Supplementary Fig. 2 a,b). A pneumatic control system was set up for the model's operation (see Supplementary Note 1 and Supplementary Fig. 3).

Bolus transport through the esophagus (Fig. 1b) has three stages: passive, pre-bolus, and post-bolus. In the pre-bolus stage longitudinal muscles contract, increasing circumferential muscle concentration [37]. The circumferential muscles then contract radially, forming a region of high pressure [34]. The opposite occurs in the post-bolus stage, creating a region of low pressure [34]. Remaining regions are in a pressure-neutral passive state. The method of simulating these three stages with the soft-robotic model is shown computationally (Abaqus, Dassault Systèmes) in Fig. 1b. Pressurization of all chambers to a mid-pressure (half the pressure used for the pre-bolus stage) replicates the passive stage. This no-load condition, where the chambers are at half-peak pressures, is referred to as the model 'passive' state. Decreasing the pressure in the longitudinal chambers and increasing it in the circumferential chambers replicates the pre-bolus stage. The opposite then results in the post-bolus stage.

To demonstrate model versatility, we perform three studies (Fig. 1c): (1) stent migration under a 'simple swallowing wave', (2) the effects of bolus viscosity on HRM diagnosis of achalasia, and (3) the swallowing efficiency of mixed and unmixed Greek-style yoghurt under achalasia types II and I. In these studies, porcine esophageal tissue was incorporated (Supplementary Fig. 2c), running through the model's inner lumen which, aided by the model's hexagonal shape, further mimics the esophageal environment (Fig. 1d). In any studies without tissue, the model is referred to as RoboGullet as opposed to RoboGullet+.

Computational design of soft-robotic structure

The internal lumen of the esophagus is not a perfect circle. It consists of 4-6 folds [38], along which it buckles and gives it a polygon-like shape in its passive state [38], which significantly affects bolus flow [39]. To replicate this, we conducted a study to see which shape best matches the porcine esophagus in its passive state (Fig. 2a). FEA was used to simulate pneumatic actuation of a soft-robotic model segment with shapes ranging from 0 (circle) to 6 folds (hexagon). Lumen surface areas at the model 'passive' state was mapped (MATLAB) and compared to porcine esophageal [38] through Dice-Sørensen similarity coefficient (DSC) for area (Fig. 2b) [40] and the turning distance for shape (Fig. 2c) [41]. The highest turning distances were hexagon (0.77) and triangle (0.82), with hexagon also scoring highest in DSC (0.83) and was thus chosen for the design.

The circumferential chambers for radial displacement, based on Chen et al. [42], and the longitudinal chamber, designed as bellows for axial displacement (Supplementary Fig. 1), were tested for independent actuation. An FEA model (Abaqus, Dassault Systèmes) was used to study independence of the proposed chambers and inform material selection (Fig. 2d). The circumferential and longitudinal chambers were inflated to half their peak pressure (model 'passive' state), then the circumferential inflated to peak pressure while longitudinal held constant, and finally the longitudinal inflated to peak pressure while circumferential held constant. The displacement in the middle of the lumen surface was tracked over time. Initially, EcoFlex 00-30 (Fig. 2d) was used for the whole model as this has similar properties to gastrointestinal tissues [43]. The resulting post-decoupling axial displacement shows a correlation coefficient of 0.64, meaning there is a lack of independent behavior (Fig. 2e). Replacing the longitudinal chambers with DragonSkin 20 (Fig. 2d) improved independence, with a correlation coefficient of 0.98 indicating the achievement of independent actuation (Fig. 2f).

Computational and experimental characterization of the soft-robotic model

A scaled version of RoboGullet (10 segments) was created in Abaqus (Dassault Systèmes) with a HRM catheter (ManoScan ESO 3D, Given Imaging) [44] (Fig. 3a). This setup was then recreated experimentally (Fig. 3b). For both, pressure data along the manometry catheter was captured during a swallow (Fig. 3c) (wave settings discussed in Supplementary Note 2), and the computational data interpolated [45]. The resulting computational HRM topography plots were imported into MATLAB and processed to match length and timescales. To compare these plots, pressure vs time curves were extracted at four intervals along the catheter [46] from upper to lower pressure topography plot peaks (Fig. 3c). Mean amplitude of contraction and wave velocity, commonly used to describe a swallow wave [47], were chosen as comparison parameters. Wave patterns differ slightly due to computational simplifications but trends match – the computational model predicted the experimental mean amplitude of contraction (117.81 ± 12.32 mmHg) and the wave velocity (4.16 ± 0.04 cm/s) with a computational accuracy of 95.14% and 89.70% respectively when compared to the experimental data.

Soft-robotic model predicts stent migration in a design dependent manner and the effect of physiological factors

A simple swallowing wave (Supplementary Fig. 4c), meaning one excluding UES/LES simulation to allow for linear migration tracking without interference, was simulated for this study – the HRM plots of the input PID regulated wave, and corresponding PWM input wave are shown in Fig. 4a. These simulated swallows parameters, detailed in 'Computational and experimental characterization of the soft-robotic model', fit within those of normal swallowing waves [11]. Six commercially available stents with either partial (PC) or full covering (FC) were evaluated (Fig. 4b) from two brands. The type, outer diameter (OD), and length (L) for each stent are detailed in Supplementary Table 1. Brand A is a multiple nitinol wire braided construction [48] and Brand B is a dual-gauge nitinol wire construction [49]. Stents were deployed just below the midpoint of the initial model segment and subjected to 30 simulated swallows (n = 5). Stent displacement was tracked with a tethered washer (6.4g). Both RoboGullet (Fig. 4c) and RoboGullet+ (Fig. 4d) were used. Images of stent start and endpoints are shown in Fig. 4e-f, and intermediate images in Supplementary Movie 2.

In RoboGullet, Brand A stents displaced significantly more (Stent I = 20. 5 ± 4.3mm, Stent II = 25.9 ± 1.4mm) than Brand B (Stent III = 4.0 ± 0.9mm, Stent IV = 5.3 ± 4.5mm, Stent V = 1.7 ± 0.3mm) ($p = 0.0383$). The regression model in Fig. 4g shows changing brand as the only statistically significant parameter, with an expected 20.1mm displacement decrease when switching from Brand A to B.

Adding tissue (RoboGullet+), increased displacement in Stent II by 24.3 ± 11.7mm, Stent IV by 2.9 ± 4.9mm, and Stent V by 9.1 ± 3.5mm. It decreased in Stent I by 18.9 ± 4.3mm and in Stent III by 2.0 ± 1.5mm. Stent migration is influenced by multiple factors; our model helps disentangle these factors to inform improved stent designs. Tissue is particularly important when comparing the migration of PC, which aim to reduce migration through tissue interaction [6], and FC stents. Since Stents III and V's only variation is this covering, this can be used to illustrate the importance of the biohybrid approach (Fig. 4h), whereby when tissue is added the FC version's displacement significantly increases ($P < 0.005$), while the PC version decreases. Despite this, a regression analysis performed for RoboGullet+ revealed no statistically significant parameters.

Combining circumferential and longitudinal pneumatic actuation significantly increased displacement ($P < 0.001$) (Fig. 4i.). Stent I was evaluated under isolated circumferential and longitudinal actuation ($n = 5$). The stent displaced 20.5 ± 4.3mm under the original combined muscle conditions, compared to the 3.8 ± 5.7mm and -0.1 ± 0.3mm under these circumferential and longitudinal isolated conditions, respectively.

Soft-robotic simulation of achalasia subtypes and effect of bolus viscosity on their diagnosis and dietary recommendations

Swallows mimicking normal and three types of achalasia were simulated with RoboGullet+ using the pneumatic inputs in Supplementary Fig. 5-6. These swallows are more complex than that used for stent migration studies, as these include the UES and LES (simulated with 1st and 16th model segment respectively – functional, not anatomical, simulation was prioritized as there are no major histological differences between UES/LES and esophageal body [50,51]). A ManoScan ESO manometry catheter (Given Imaging) was inserted in the model and swallows recorded using ManoScan Acquisition. The resulting HRM plots (Supplementary Fig. 7 – 15) were analyzed in ManoView ESO to extract the diagnostic metrics [11] (labelled in Fig. 5a): distal latency (DL), integrated relaxation pressure (IRP), and distal contractile integral (DCI).

The clinical standard for achalasia diagnosis, the Chicago Classification 4.0 [11], gives thresholds for these metrics which define normal and achalasia swallows (Fig. 5, b-d, dashed lines and grey fill). The measured mean metric values for swallows under the typical 5mL water bolus [11] are shown in Fig. 5b–d. Both mean and standard deviations for DL, DCI, and IRP in all four simulated states lie within the thresholds, showing successful simulation. Omissions, such as achalasia type II with DCI (Fig. 5c), occur because that metric is not applicable in its diagnosis [11].

The effect of bolus viscosity on these metrics was also investigated. Newtonian solutions (50, 62.5, 75, 87.5, and 100 wt% glycerol in water) were used, alongside non-Newtonian solutions made from a commercial dysphagia thickener mixed with water at levels commonly used by patients (0.6, 1.35, 2.1, 2.85, and 3.6 wt%) [52] and equivalent to thin-to-honey viscosities as per the National Dysphagia Diet [52,53].

Only DL was notably affected. In normal swallows (Fig. 5e), DL remained relatively stable with increasing viscosity for both solutions, except for the non-Newtonian bolus at higher viscosities. Here, DL drops from 6.6 ± 0.1s at 2.1wt% to 4.1 ± 0.0s and 4.4 ± 0.1s at 2.85wt% and 3.6wt% respectively. A similar downward trend is observed with the non-Newtonian solution in the achalasia type III swallows (Fig. 5f), decreasing by 20.8% over the entire range. The Newtonian solution sees little effect until 87.5wt% and 100wt%, when DL drops from 2.8 ± 0.2s to 1.8 ± 0.9s and 0.6 ± 0.1s respectively. As IRP (Fig. 5, g-i) and DCI do not change significantly, these trends suggest that in mild achalasia type III cases, where the DL is close to normal (4.5s), increasing bolus viscosity could improve diagnosis rates.

Yoghurt is a common dietary recommendation for patients with achalasia [54]. Seeing the lack of effect viscosity change had in diagnosing the more severe achalasia type II and I, we evaluated how changing the viscosity of yoghurt through stirring would affect bolus transit. The 9th segment was contracted pre-swallow to reduce travel distance. Unstirred (US) and stirred (S) yoghurt was injected above this. Swallows were carried out in a worstcase scenario with no LES relaxation (n=5). The weight of the bolus extruded was tracked from swallow initiation over 5 minutes. Stirring significantly improved bolus passage for both types of achalasia ($P < 0.05$) (Fig. 5j).

Discussion

In this work, we describe a soft-robotic model with tunable esophageal motility simulation through independent actuation of the UES, LES, and circumferential/longitudinal muscles. This was achieved through a dual-material solution, involving computational design (Fig. 2), bespoke lost-wax fabrication (Supplementary Fig. 2 a,b), and a pneumatic control system. A biohybrid approach was employed by fixing porcine esophageal mucosa/submucosa within the model lumen (Supplementary Fig. 2c). The model was used to investigate stent migration, and bolus viscosity effects on achalasia diagnosis and swallowing.

When investigating or simulating peristaltic motion the longitudinal muscles are often overlooked, with focus instead being on the circumferential muscles [34]. This is despite clear evidence that coordination between the two muscles is critical to normal peristaltic function [55] and that the longitudinal muscles play a critical role in the development of motility disorders [33], which itself remains incompletely understood [12]. The only other GI model to-date incorporating longitudinal muscles [26] leaves the model axially unconstrained, causing axial displacement during radial contraction. The resultant lack of independence, however, limits the utility of the platform in device and disease evaluation, where the desired contraction of muscles may not be synchronous or vary in amplitude [34]. Our platform can achieve independent localized control of both muscle groups, though use of a dual-material design, as demonstrated computationally (Fig. 2d) with a correlation coefficient of 0.9837 versus 0.6409 for a single-material approach.

Stent migration is challenging to predict due to patient variability. Our soft-robotic model offers a consistent platform to evaluate how stent design and environment affect migration. Consistent with published findings [8], we found brand significantly affects migration. Friction is also critical in predicting migration [56]. Unlike other platforms that use liquids to mimic esophageal friction [23,26], we incorporate porcine esophageal tissue lining (RoboGullet+). Porcine mucosa is often cited as a valid surrogate for human tissue, with comparable morphology, permeability, and biomechanical responses [57–61]. While ex-vivo porcine tissue may differ slightly from in-vivo, for example in levels of hydration, studies show minimal biomechanical alterations [62,63]. This tissue addition led to increased displacement in FC stents and decreased displacement in PC stents, better aligning with clinical findings [64–66] and indicating that friction mismatches in models may misrepresent migration. Migration may also be misrepresented in current models due to the continual omission of longitudinal muscles representation in its evaluation. Our model, when actuated with isolated circumferential muscles, saw a fivefold decrease in the migration of a commercially-available FC stent (Stent I) when compared to combined circumferential and longitudinal muscles. Additionally, our model, when actuated with isolated circumferential muscles (Fig. 4i), shows localized positive and negative displacement regions similar to Bhattacharya et al.'s circumferential model [23] when using comparable stents (Stent A and Stent I) and velocities (4.12 vs 4 cm/s).

Our model's ability to simulate tunable longitudinal muscle function opens, for the first time, the possibility to simulate motility diseases, such as achalasia, in which these muscles play a crucial, interrelated role. In achalasia II, only the longitudinal muscles contract, causing pan-esophageal pressurization [67]. This is theorized to result from reduced esophageal volume [33,67]. Simulating this scenario in RoboGullet+ yields swallowing waves that meet the diagnostic threshold for achalasia II [11], supporting this theory. Using a single pneumatic input formula (Supplementary Note 2), we successfully simulated normal swallows and achalasia types I-III by adjusting only wave velocity (v_w), contraction time (λ), and contraction amplitude (A). This strongly supports the unproven "Pavlova Theory", which theorizes achalasia progresses from mild (Type III) to intermediate (Type II) to severe (Type I) [67–69]. Combining RoboGullet+ with HRM could yield more robust achalasia diagnostic criteria based on continuum rather than discrete disease types.

The current, standard paradigm of esophageal manometry [11] focuses on water swallows [70], which can often result in inconclusive diagnosis [71], although viscous and solid swallows are also suggested as adjunctive, provocative tests [11]. The effects of varying viscosity of Newtonian and non-Newtonian boluses have been studied with a benchtop model in the pharynx [72], but not to the same extent in the esophagus. Clinical studies have typically been limited to one-to-one comparisons, such as water versus apple sauce [13] or solid food [71]. Using non-Newtonian boluses, we observed large decreases in DL for normal and achalasia III swallows when viscosity increased , even shifting a normal swallow to a premature one[11] (Fig. 5e). These trends mirror clinical observations, where apple sauce (non-Newtonian) significantly reduced mean wave velocities [13] without affecting IRP, suggesting patients with borderline DL (near 4.5s) might be more accurately diagnosed using a viscous non-Newtonian bolus. Notably, misinterpretation seen with Newtonian bolus in achalasia III, where weak contractions and increased viscosity cause a near-instantaneous wavefront misclassified as achalasia II, is absent with the non-Newtonian bolus. Additionally, our findings on stirring yoghurt prior to consumption by severe achalasia patients highlight viscosity's importance for dietary recommendations and the influence the model can have on evidence-backed recommendations.

Our work demonstrates our model's versatility simulating esophageal motility, offering potential in medical device evaluation and clinical practice. It bridges the gap between benchtop and *in-vivo* evaluation of stents, viscous and topical/nebulized treatments [73], post-swallow 'smart pills' orientation [74], and electromyographic wearables [75].

Clinically, the platform enables controlled transitions between motility disease states, potentially refining achalasia diagnostics beyond current Chicago Classification guidelines [11]. Beyond achalasia, the device can simulate other motility/inflammatory disorders, such as hypercontractile esophagus, distal esophageal spasm, eosinophilic esophagitis, and transient lower esophageal sphincter relaxation. As demonstrated in our swallowing efficiency study, this platform could provide new insights for dietary recommendations which, for dysphagic patients, are largely based on clinical experience rather than scientific evidence. The use of 3D printed parts for molding enables future patient-specific esophageal models, with anatomy replicated from CT scans, for treatment planning, such as LES myotomy, and offers a more biomimetic platform for endoscopic training. Additionally, the model's 'passive' state could be adjusted for lumen/strictures. The model's versatility permits training for multiple scenarios rather than the limited conventional roller systems [76]. Finally, integrating emerging neuromechanical esophageal models [77] with the model's feedback system could advance understanding of motility disorders.

Despite its advantages, our platform has limitations. First, discrepancies between input and output wave velocities arise when transitioning from PID to PWM inputs due to the Arduino's low clock speed. Although this did not affect our study (final velocity was measured diagnostically), future iterations could implement more powerful microcomputers which would also facilitate algorithms to convert HRM topography plots into patient-specific pressure inputs, enhancing clinical utility. This would allow clinicians to pre-test treatments on patient-specific swallows. Full-scale in-depth studies with larger sample sizes, using animal model or clinical data for validation, are needed to fully verify our findings. However, obtaining quantitative clinical data upon the onset of stent migration remains challenging, but could be achieved through emerging smart sensor technology [74]. Model wall thickness is larger than esophagus muscle; this may overestimate stiffness and thus stent migration. Despite this, thicker EcoFlex 00-30 remains an excellent analog for GI tissue [43], and the comparison of stents under identical conditions means migration trends remain valid. In our model, we approximate the loose connection of the submucosa, which allows movement between mucosa and muscularis [78,79], through fixed constraints of the mucosal tissue at either end of the model, frictional interaction along its length, and model pre-tensioning. This does not fully capture the intricacies of connective tissue attachment, particularly in the radial direction, but similar to computational approaches [78], aims to replicate its functional role. Finally, while ex-*vivo* tissue incorporation offers demonstrated benefits, its feasibility in larger studies requires further exploration.

Our soft-robotic model provides a versatile platform for understanding esophageal motility and its treatments. Our studies demonstrate valuable proof-of-concept insights on stent migration and dysphagia that are not achievable through conventional *in vivo* assessment.

Methods

Study design

This study aimed to develop and demonstrate the versatility of an esophageal model that more accurately describes esophageal motility through simulation of both circumferential and longitudinal muscle groups. This model's inner geometry was based on the average diameter of the esophagus from literature [50] and shaped to mimic mucosal folding seen in an esophagus [38,39]. A dual-material model (softer EcoFlex 00-30 (circumferential) and stiffer DragonSkin 20 (longitudinal) for independent actuation) was developed to achieve independence between circumferential and longitudinal muscle movement, requiring a bespoke lost-wax casting procedure to be molded. The model was used to carry out three studies under various differing swallowing conditions. Each of these swallowing conditions was defined by values given in the Chicago Classification 4.0 [11] and validated using high resolution manometry (Sierra Systems, ManoScan). Firstly, the model was used to evaluate stent migration over 30 normal swallowing cycles with a 5mL bolus of water. This was the only study in which the UES and LES were excluded. The displacement of 5 commercial stents in RoboGullet and RobotGullet+ was tracked using a washer (6.4g) hanging from the stents by a suture being imaged post-swallow. Migration of one stent was also evaluated with isolated circumferential and longitudinal muscle activation. Secondly, RoboGullet+ was used to evaluate the effect of bolus viscosity on the diagnosis of swallowing under achalasia conditions. Boluses used were water, glycerol mixed with water (50%wt, 75%wt, and 100%wt) and ThickenUp mixed with water (0.6%wt, 2.1%wt, and 3.6%wt). The swallows were recorded using HRM (ManoScan) and values for IRP, DCI, and DL were obtained using ManoScan ESO Analysis. Lastly, RoboGullet+ was used to investigate swallowing efficiency for non-Newtonian boluses (mixed/unmixed Greek yoghurt) under severe achalasia types I and II. Swallowing efficiency was measured as the weight of bolus passed through the model.

Model geometry and computational design.

The model dimensions, seen in Supplementary Fig. 1, were based on the average esophageal dimensions (20mm ID, 32cm length) [50]. The circumferential pneumatics were based on that proposed by Bhattacharya et al. [23] and other foundational work by the Xu group [80,81], and the longitudinal chambers that of a bellows [35]. These internal dimensions are also described in Supplementary Fig. 1. EcoFlex 00-30 was selected for circumferential chamber use due to its similar properties to gastrointestinal tissues [43].

In order to select the material to be used for the longitudinal pneumatic chambers, a portion of the model (5 segments) was modeled and simulated in Abaqus Explicit with the entire model made of EcoFlex 00-30 and then with the longitudinal chambers made from DragonSkin 20. The material properties for both materials were modeled using a hyperelastic Ogden model [82] (Supplementary Table 2). The model was inflated to the midpoint over 2 seconds, then the circumferential chambers inflated to maximum pressure, while longitudinal chambers were held constant over 2 seconds, and then the longitudinal chambers inflated to maximum pressure with the circumferential held constant. To achieve a wave shape, the maximum pressure of each circumferential chamber was set to 12.5kPa, 16kPa, 20kPa, 16kPa, and 12.5kPa respectively for both studies. Longitudinal pressures were tuned for equivalent axial displacement in the passive state (Supplementary Fig. 16). The max pressure for each longitudinal chamber during the EcoFlex only study was 2.375kPa, 3kPa, 3.75kPa, 3kPa, and 2.375kPa respectively. The max pressure for each longitudinal chamber during the DragonSkin study was 36.894kPa, 51.782kPa, 64.727kPa, 51.782kPa, and 36.894kPa respectively. The displacement of a node in the middle on the surface of the model was tracked.

The number of folds in the human esophagus is between 3 and 6 [38,39]. To decide on the optimum shape to replicate these folds, a single segment of the model was modeled and simulated in Abaqus Explicit in five different shapes: a circle, a triangle, a square, a pentagon, and a hexagon. A symmetry condition was applied to either side of the segment. 50 kPa of pressure was applied to the circumferential chamber over 2 seconds. Images were taken at the midpoint of closure (1/2 the time to full closure). The resulting images were compared to the shape of the inner lumen of an esophagus [38] by converting them to a boundary and calculating the Dice-Sørensen similarity coefficient (DSC) using MATLAB.

The final model design was computationally validated by simulating a section of the model (10 segments) undergoing a manometry procedure in Abaqus Explicit. A tube matching the dimensions and sensor arrangement of a 4.2mm OD Sierra solid-state manometry catheter [44] was placed within the model ‘tract’. Manometry catheter set as a stationary rigid material due to relative difference in material stiffness (Young's modulus (190 GPa) and density of 1.07×10^{-9}). Ogden model (Supplementary Table 2) used again for DragonSkin 20 and EcoFlex 00-30. A step of 1 second was used for the model to inflate to the midpoint, and then the swallow step was carried out over 12.6. The Von Mises stress and equivalent strain in two groups of central EcoFlex 00-30 elements were tracked up to the midpoint/'passive state' (Supplementary Fig. 17). This revealed negligible change in instantaneous Young's modulus (0.14%) from 'relaxed' to 'passive' states. 'Simple' swallowing wave (Supplementary Fig. 4c) then simulated and contact pressure was tracked over pressure sensing catheter areas [44]. A general contact with frictionless condition was used over the entire model, and a surface-to-surface contact was used between the 'tract' wall of the esophageal model and the catheter with a friction coefficient of 0.213 [83].

Pressure data extracted using a Python script (Supplementary Note 3), interpolated with the same methods forming the basis of those used by manometry software [44,45], and plotted in the form of manometry graphs [45]. The resulting plots were then compared to experimentally obtained HRM swallowing data. Velocity taken as time between peak pressures at initial/final points over distance. Amplitude taken as baseline-peak average across four evenly spaced points [46].

Model and pneumatic control board fabrication.

The molds for the beeswax cores, consisting of an outer shell and circumferential and longitudinal chamber positives, were 3D printed using a Form 3 SLA printer (Formlabs). Steel rods (3 mm OD, TOPPROS) inside silicone tubing (McMaster-Carr, 1/8" ID, ¼" OD) held the positives in place within the mold. MoldStar 60 silicone (SmoothOn) was degassed for 15 minutes, poured into the mold, and cured in a pressure pot at 4.48 bar. Once cured, the positives, rods, and tubing were removed. To create the wax cores for the model, a base and lid with a hole for pouring into the mold were laser cut (Geike Cloud 50W CO2 laser) and screwed to the mold. Beeswax (Vanrener) melted in an oven at 80 °C, was poured in and cooled to room temperature, thus creating wax cores.

To create the EcoFlex portion (inner circumferential chambers), 3D-printed inner segments were stacked and secured with M3 threaded rods (316 Stainless Steel, McMaster-Carr) and nuts (McMaster-Carr) to a laser-cut acrylic base. EcoFlex 00-30 parts A and B were mixed, degassed for 30 minutes, poured into the mold. After 4 hours, the part was removed from the mold. Using IPA as a lubricant, circumferential wax cores were inserted into position on the EcoFlex part. Two of the 3D-printed inner segments were inserted at either end of the EcoFlex part and held in place with 28cm M3 threaded rods and M3 nuts (McMaster-Carr). This was mounted to the laser cut acrylic base of the DragonSkin 20 leaving a 15mm gap between the base and EcoFlex part.

192 pieces of 4cm long high-purity silicone tubing (McMaster-Carr, 1/8" ID, ¼" OD) were roughened with emery sheets (P80, RS Pro). The tubes, held upright on a 3D printed base (Form 3, Formlabs), were cleaned with IPA and compressed air and placed into a plasma chamber (Harrick Plasma PDC-32G-2). The tubes were treated with air (ECVP4300, Easy Composites Ltd) for 3 minutes on high, the vacuum released and then reestablished for a further 3 minutes.

The DragonSkin mold (outer longitudinal chambers) was assembled sequentially, with each segment being stacked and secured with six 37cm 10-24 threaded rods (316 Stainless Steel, McMaster-Carr) and nuts (McMaster-Carr). Three laser cut acrylic pieces of 5 mm thickness (bottom endcap) were stacked first, followed by symmetrical 3D printed (Form 3, Formlabs) DragonSkin mold segments. The vacuum was released in the plasma chamber, and the 6 pieces of silicone tube removed. A 3mm OD rod approximately 50mm in length (Stainless Steel, TOPPROS) was inserted into each of these tubes, inserted into the longitudinal wax cores onto the DragonSkin segments. Three of the tubes with rods were then further pushed into the circumferential wax core. Silicone adhesive (MED3-4013, NuSil) was brushed (Size 4 round, Winsor Newton) onto the tubing before repeating the process another 15 times. Finally, 3 laser cut pieces of 5 mm acrylic were placed on top (top endcap) and the mold tightened with 10-24 hex nuts (McMaster-Carr).

DragonSkin 20 (Smooth-On) parts A and B were mixed, degassed for 15 minutes, poured into the mould, and cured under in a pressure pot (2 bars) for >4 hours. After demolding and removal of the steel rods, the part was placed in an oven (LHT 6/30, Carbolite Gero) at 90 °C to melt out the wax. After the wax had melted out, the part was submerged in boiling water and then cleaned with compressed air.

Where indicated (RoboGullet+), porcine mucosal/submucosal tissue was added to the model. Tissue was sourced from Wetlab-Medmeat for migration studies and MIT for motility studies. The tissue was flushed with physiological saline and its length measured. The esophageal layers were separated following the process laid out Durcan et al. [58] and the tissue frozen. When subsequently used, the tissue was defrosted in room temperature physiological saline. This approach of using of frozen/thawed tissue over fresh tissue, the procurement of which limits model utility, is one used by other biohybrid models [84–86].The tissue was placed over a steel rod (12mm OD, 31.5cm length) and fed through the model. Four equally spaced longitudinal cuts, about 2cm in length, were made at the distal end of the tissue. These were stapled (26/6) to the bottom of the model. The tissue was then pulled to its original length, and four equally spaced longitudinal cuts were made at the proximal end. These were stapled to the top of the model and any excess tissue trimmed. The submucosa, composed of loose connective tissue, separates the mucosa from the muscularis and allows the mucosa to move freely [78,79]. As the model simulates the muscularis, we replicated this interlayer movement by excluding model-mucosal tissue adhesion between stapled sections. Pre-tension in 'passive' state (1.54 ± 0.00 strain, comparable with reported in-vivo axial strain is 1.35-1.5 [39,87]) was recorded across one of each normal and achalasia I-III swallows. It was calculated by imaging (EOS R5, Canon) the model in its 'passive' state with tracking markers and digitally measuring displacement (ImageJ).

Friction testing was carried out between nitinol and the mucosal surface of esophageal tissue that was frozen/thawed, both before and after use in stent migration testing, to confirm no change in its mechanical performance (Supplementary Fig. 18). Experimental setup (Supplementary Fig. 18a) was based on ISO 8295-1995 (200g weight and 20cm^2 sample surface area) which has been used for soft-tissue friction testing [88]. A rubber gasket was used for tissue fixation. An average sliding speed equivalent to that of peristalsis (0.5 mm/s [89]) was used, with resistive force measured via a tensile tester (10N load cell, SL1 Lloyds). Trip displacement was 22mm [61]. The onset of sliding, used for static coefficient measurement [90], was defined as when change in force over displacement dropped below 0.002 N/mm. Static coefficient of friction of tissue after use in stent migration studies (0.08 ± 0.01) was not significantly different from before use (0.09 ± 0.02)p = 0.275). Friction coefficients are similar to values of 0.1 reported in literature for fresh porcine esophageal mucosa [56,61].

The soft-robotic model is pneumatically actuated using a general compressed air supply. The compressed air supply is connected to a 2-port valve (VHK2, SMC Pneumatics) via 6mm OD tubing (PUN-6X1-BL, Festo). This is then in turn connected to a pressure regulator (0.05 – 0.89 MPa, AP100, SMC), a flowmeter (10 L/min – 100 L/min, RS PRO), a pressure relief valve (0.3bar to 7bar, NORGREN), and two manifolds (VV100-41-18-M5 and VV100-S41-14-M5, SMC Pneumatics) via push-in fittings (M5 to 6mm, Festo) connected in series, all elements being connected with the same type of PVC tubing. 32 solenoid valves (V114-5LZ, SMC Pneumatics) are mounted on these manifolds to control the air flow. Each output from the manifold corresponds to an individual solenoid valve. These are connected to the relevant chambers of the model via lines of tubing (ADF00011, TYGON® ND 100-65, Saint-Gobain Medical), that separate into two via a wye connector barb (4/16” ID, McMaster-Carr), and into its relevant chamber on the soft-robotic model via a straight connector (3/16” ID, McMaster-Carr). Each chamber in the soft-robotic model has an additional port from which a PVC tube runs via a straight connector (3/16” ID, McMaster-Carr) to connect to 32 pressure sensors (0 – 700kPa, MPX5700GP, NXP USA Inc.).

In terms of the electronics of the system (Supplementary Fig. 3), a microcontroller (MEGA 2560, Arduino) is used to control the pneumatic setup. It is connected to two PWM drivers (16-Channel 12-bit PWM/Servo Driver, Adafruit). These are then connected to 8 MOSFETs (4 Channel IRF-540, Gump’s Grocery) which connect to the solenoid valves. The pressure sensors all run through two 16 channel multiplexers (BOB-09056, SparkFun Electronics) to connect back to the Arduino. Arduino is also connected to a micro-SD card reader (HiLetgo). All electronic components run off either 24V or 5V. 24V power comes from a wall mount DC power supply (L6R48-240, Tri-Mag LLC) and 5V power stepped down from the 24V power via an adjustable DC-DC buck converter (LM2596S, Frienda). The only component that is not powered through these channels is the Arduino, which is powered via USB.

Evaluation of stent migration.

A study of stent design and its impact on migration was conducted using five different commercially-available stents (expired stock samples available from eSutures) with RoboGullet and RoboGullet+. Variations in brand, covering, and outer diameter (OD), were considered. 30 sequential ‘simple’ swallows, or healthy swallows excluding UES or LES, were simulated (Supplementary Fig. 4c). The soft-robotic model was placed on a box with a panel on its side cut out for imaging the washer. A manometry catheter (ManoScan ESO 3D, Given Imaging) was inserted into the model lumen and a PID regulated swallow simulated, with PWM values recorded to be used for subsequent swallows. Imaging was carried out with a camera (EOS Rebel T6 with EF-S 18-55mm f/3.5-5.6 IS II lens, Canon) mounted on a tripod (Star 62, Hama) for a lumen view and phone camera (XQ-AS52g, Sony) mounted to a lab tripod for laterally imaging the washer. The phone’s orientation was aligned using a spirit (T3482, CK Tools). A suture line (W328H Mersilk, Ethicon) was tied to each stent. Each stent was placed at the midpoint of the first onset segment via tubing (10mm OD). A washer (6.4g) with a 3mm reflective marker (Revopoint) was attached to the external portion of suture. For each swallow, 5mL of water was injected upon relaxation wave initiation. The model was programmed to stay in its 'passive' state for 20 seconds in between each swallow. During this 'passive state', where all model-chambers are held at half-peak pressure, washer displacement was automatically imaged through a timelapse set to image once per swallow (Velocity Lapse v1.1.0 PRO using Sony XQ-AS52g phone camera) and luminal images captured manually (EOS Rebel T6, Canon). As the model remains fixed in position during this 20s period, images taken of washer and lumen are synchronized. Luminal images taken of the stents are included in Supplementary Movie 2. After each set of swallows, if displaced, the stent was repositioned. Tests with RoboGullet+ included 5mL injections of physiological saline after each swallow and a 20mL injection after stent removal.

Achalasia simulation and effect of bolus viscosity on swallow diagnosis and efficiency

Further versatility of the model was demonstrated by using RuboGullet+ to simulate normal and achalasia swallows that incorporate the UES and LES. The Newtonian bolus used was glycerol-water (50wt%, 62.5wt%, 75wt%, 87.5wt%, and 100wt%). The non-Newtonian bolus used was a commercially available dysphagia thickening powder, which uses xanthan gum as its main thickener and maltodextrin as an excipient [52]. This was mixed with water over a commonly used range of 0.6wt%, 1.35wt%, 2.1wt%, 2.85wt% and 3.6wt% [52], equivalent to thin-to-honey viscosities [52,53]. A bolus of water was used for validation of the swallows against clinical metrics and for comparison with viscous boluses.

A manometry catheter (ManoScan ESO, Given Imaging) was placed inside the model lumen and held with a lab tripod. Before each swallow the UES position was shifted to the 4th segment, contracted to closure for 40 seconds, and 5mL of bolus injected into the space above (Supplementary Fig. 5-6). 5 seconds before swallow initiation the UES is switched back to the 1st segment. The only exception to this was the achalasia II swallow, where there was no gap before swallow initiation. Originally, a different waveform was used for this swallow (Supplementary Fig. 6) with a slower contraction (λ = 12s) and lower setpoint pressure. However, this failed to produce pan-esophageal pressurization and was replaced with a faster contraction (λ = 3s) and higher setpoint pressure (1.7 times). HRM data was recorded with ManoScan Acquisition (Medtronic). After each change of condition, the manometry catheter was removed and wiped. Additionally, 20mL of physiological saline was injected into the model lumen and a steel rod (12mm) inserted through the lumen to flush out any remaining bolus. Data was analyzed using ManoScan Analysis ESO 3.0. where DL and DCI, was calculated automatically. IRP (median of lowest pressures over 4 seconds [11]) was taken to be the LES residual pressure (mean of lowest pressures over 3 second time period [91]), as IRP was not given as an output in the program.

An additional study was examined the effect of non-Newtonian dietary recommendations like Greek-style yoghurt [54] has on dysphagic swallowing efficiency. The Greek-style yoghurt (Natural set, Onken) was refrigerated, then stirred before each swallow or left unstirred. RoboGullet+ was placed on the top housing of a weighing scale (Pioneer Precision, OHAUS) with a custom draft-shield with a 20mm OD hole aligned to the lumen.

Scale data was collected at 1s intervals starting at swallow initiation via a USB to 9-pin RS232 Serial Port Adaptor (Aten Technology). Achalasia II and achalasia I swallows were simulated without LES relaxation. Closure of the 9th segment was used for filling to reduce transit time. Here 5mL of yoghurt was injected. After each swallow, 20mL of physiological saline was injected to flush out remaining bolus.

Data Analysis

All plots were made using MATLAB and Excel. Correlation coefficients were calculated using MATLAB. All of the HRM data was recorded with ManoScan Acquisition and analyzed using ManoScan Analysis ESO 3.0. Computational predications were compared to physical model predictions using a custom Python script for HRM plot generation (Supplementary Note 3), combined with MATLAB for image analysis. For the stent migration studies, Kinovea was used to get the displacement data from the timelapse videos. Multiple linear regression model fit and analysis was carried out using MATLAB. A two-tailed t-test was used for comparison of FC and PC Brand B stent migration. A two-tailed t-test was used for comparison of tissue friction properties. A right sided t-test was used to test significance of circumferential and longitudinal muscles in stent migration. For the swallowing efficiency of yoghurt, a left-sided Mann-Witney test was used as the data for one of the groups was not normalized. Significance threshold: $P<0.05$ (unless otherwise noted). The scales were data logged using Serial Port Data Collection Software (SPDC V2.04, OHAUS).

Data Availability

The authors declare that the data supporting the findings of this study are available within the paper and its supplementary information files. Any additional requests for information can be directed to the corresponding author. Source data is provided with this paper.

References

1. Meyer, G. W. & Castell, D. O. 1 - Physiology of the Oesophagus. *Clin. Gastroenterol.* **11**, 439–451 (1982).
2. Patel, D. A., Yadlapati, R. & Vaezi, M. F. Esophageal Motility Disorders: Current Approach to Diagnostics and Therapeutics. *Gastroenterology* **162**, 1617–1634 (2022).
3. Adkins, C. *et al.* Prevalence and Characteristics of Dysphagia Based on a Population-Based Survey. *Clin. Gastroenterol. Hepatol. Off. Clin. Pract. J. Am. Gastroenterol. Assoc.* **18**, 1970-1979.e2 (2020).
4. Pandolfino, J. E. & Gawron, A. J. Achalasia: A Systematic Review. *JAMA* **313**, 1841 (2015).
5. Mitra, T. *et al.* Clinical profile of patients presenting with dysphagia - an experience from a tertiary care center in North India. *JGH Open Open Access J. Gastroenterol. Hepatol.* **4**, 472–476 (2019).
6. Sharma, P. & Kozarek, R. Role of Esophageal Stents in Benign and Malignant Diseases. *Am. J. Gastroenterol.* **105**, 258–273 (2010).

7. Vleggaar, F. P. & Siersema, P. D. Expandable Stents for Malignant Esophageal Disease. *Gastrointest. Endosc. Clin. N. Am.* **21**, 377–388 (2011).

8. Thomas, S. *et al.* Fully-covered esophageal stent migration rates in benign and malignant disease: a multicenter retrospective study. *Endosc. Int. Open* **7**, E751–E756 (2019).

9. Patel, D. A. & Vaezi, M. F. Achalasia and Nutrition: Is it Simple Physics or Biology? *Pract. Gastroenterol.* (2016).

10. Patel, D. A., Lappas, B. M. & Vaezi, M. F. An Overview of Achalasia and Its Subtypes. *Gastroenterol. Hepatol.* **13**, 411–421 (2017).

11. Yadlapati, R. *et al.* Esophageal motility disorders on high-resolution manometry: Chicago classification version 4.0©. *Neurogastroenterol. Motil.* **33**, e14058 (2021).

12. Edoardo, S. *et al.* Achalasia (Primer). *Nat. Rev. Dis. Primer* **8**, 28 (2022).

13. Basseri, B. *et al.* Apple Sauce Improves Detection of Esophageal Motor Dysfunction During High-Resolution Manometry Evaluation of Dysphagia. *Dig. Dis. Sci.* **56**, 1723–1728 (2011).

14. Blonski, W. *et al.* Impedance manometry with viscous test solution increases detection of esophageal function defects compared to liquid swallows. *Scand. J. Gastroenterol.* **42**, 917–922 (2007).

15. Hirano, I. Pathophysiology of achalasia and diffuse esophageal spasm. *GI Motil. Online* https://doi.org/10.1038/gimo22 (2006) doi:10.1038/gimo22.

16. Park, C., Singh, M., Saeed, M. Y., Nguyen, C. T. & Roche, E. T. Biorobotic hybrid heart as a benchtop cardiac mitral valve simulator. *Device* **2**, 100217 (2024).

17. Dynamic Digestion Models: General Introduction. in *The Impact of Food Bioactives on Health* (eds Verhoeckx, K. et al.) (Springer International Publishing, Cham, 2015). doi:10.1007/978-3-319-16104-4.

18. Alici, G. Softer is Harder: What Differentiates Soft Robotics from Hard Robotics? *MRS Adv.* **3**, 1557–1568 (2018).

19. Slawinski, P. & Terry, B. An Automated Intestinal Biomechanics Simulator for Expediting Robotic Capsule Endoscope Development1. *J. Med. Devices* **8**, 030901 (2014).

20. Condino, S. *et al.* Stomach Simulator for Analysis and Validation of Surgical Endoluminal Robots. *Appl. Bionics Biomech.* **8**, 267–77 (2011).

21. Tharakan, A., Norton, I., Fryer, P. & Bakalis, S. Mass Transfer and Nutrient Absorption in a Simulated Model of Small Intestine. *J. Food Sci.* **75**, E339–E346 (2010).
22. Li, Y., Fortner, L. & Kong, F. Development of a Gastric Simulation Model (GSM) incorporating gastric geometry and peristalsis for food digestion study. *Food Res. Int.* **125**, 108598 (2019).
23. Bhattacharya, D., Ali, S. J. V., Cheng, L. K. & Xu, W. RoSE: A Robotic Soft Esophagus for Endoprosthetic Stent Testing. *Soft Robot.* **8**, 397–415 (2021).
24. Dang, Y. *et al.* SoGut: A Soft Robotic Gastric Simulator. *Soft Robot.* **8**, 273–283 (2021).
25. Nicosia, M. A., Brasseur, J. G., Liu, J.-B. & Miller, L. S. Local longitudinal muscle shortening of the human esophagus from high-frequency ultrasonography. *Am. J. Physiol.-Gastrointest. Liver Physiol.* **281**, G1022–G1033 (2001).
26. Peerlinck, S., Willemyns, F., Reynaerts, D. & Gorissen, B. Biomimetic Small Intestinal Peristalsis Simulator Using Circumferential Pneumatic Artificial Muscles (cirPAM). *Adv. Mater. Technol.* **9**, 2301662 (2024).
27. Jamil, B., Oh, N., Lee, J.-G., Lee, H. & Rodrigue, H. A Review and Comparison of Linear Pneumatic Artificial Muscles. *Int. J. Precis. Eng. Manuf.-Green Technol.* **11**, 277–289 (2024).
28. Ge, J. Z., Calderon, A. A. & Perez-Arancibia, N. O. An earthworm-inspired soft crawling robot controlled by friction. in *2017 IEEE International Conference on Robotics and Biomimetics (ROBIO)* 834–841 (IEEE, Macau, 2017). doi:10.1109/ROBIO.2017.8324521.
29. Park, C. *et al.* An organosynthetic dynamic heart model with enhanced biomimicry guided by cardiac diffusion tensor imaging. *Sci. Robot.* **5**, eaay9106 (2020).
30. Wirekoh, J. & Park, Y.-L. Design of flat pneumatic artificial muscles. *Smart Mater. Struct.* **26**, 035009 (2017).
31. Jung, H.-Y. *et al.* Asynchrony Between the Circular and the Longitudinal Muscle Contraction in Patients With Nutcracker Esophagus. *Gastroenterology* **128**, 1179–1186 (2005).
32. Korsapati, H. *et al.* Dysfunction of the longitudinal muscles of the oesophagus in eosinophilic oesophagitis. *Gut* **58**, 1056–1062 (2009).
33. Mittal, R. K., Hong, S. J. & Bhargava, V. Longitudinal Muscle Dysfunction in Achalasia Esophagus and Its Relevance. *J. Neurogastroenterol. Motil.* **19**, 126–136 (2013).

34. Mittal, R. K. Regulation and dysregulation of esophageal peristalsis by the integrated function of circular and longitudinal muscle layers in health and disease. *Am. J. Physiol. - Gastrointest. Liver Physiol.* **311**, G431–G443 (2016).

35. Joe, S., Totaro, M., Wang, H. & Beccai, L. Development of the Ultralight Hybrid Pneumatic Artificial Muscle: Modelling and optimization. *PLOS ONE* **16**, e0250325 (2021).

36. Edwards, C. A. & Bohlen, P. J. *Biology and Ecology of Earthworms*. (Springer Science & Business Media, 1996).

37. Brasseur, J. G., Nicosia, M. A., Pal, A. & Miller, L. S. Function of longitudinal vs circular muscle fibers in esophageal peristalsis, deduced with mathematical modeling. *World J. Gastroenterol. WJG* **13**, 1335–1346 (2007).

38. Yang, W., Fung, T. C., Chian, K. S. & Chong, C. K. Instability of the two-layered thick-walled esophageal model under the external pressure and circular outer boundary condition. *J. Biomech.* **40**, 481–490 (2007).

39. Liao, D. The oesophageal zero-stress state and mucosal folding from a GIOME perspective. *World J. Gastroenterol.* **13**, 1347 (2007).

40. Carass, A. *et al.* Evaluating White Matter Lesion Segmentations with Refined Sørensen-Dice Analysis. *Sci. Rep.* **10**, 8242 (2020).

41. Arkin, E. M., Chew, L. P., Huttenlocher, D. P., Kedem, K. & Mitchell, J. S. B. An efficiently computable metric for comparing polygonal shapes. *IEEE Trans. Pattern Anal. Mach. Intell.* **13**, 209–216 (1991).

42. Chen, F. J., Dirven, S., Xu, W. L. & Li, X. N. Soft Actuator Mimicking Human Esophageal Peristalsis for a Swallowing Robot. *IEEEASME Trans. Mechatron.* **19**, 1300–1308 (2014).

43. Miyashita, S. *et al.* Ingestible, controllable, and degradable origami robot for patching stomach wounds. in *2016 IEEE International Conference on Robotics and Automation (ICRA)* 909–916 (2016). doi:10.1109/ICRA.2016.7487222.

44. Gyawali, C. P. & Kahrilas, P. J. A Short History of High-Resolution Esophageal Manometry. *Dysphagia* **38**, 586–595 (2021).

45. Brasseur, J. G. & Dodds, W. J. Interpretation of intraluminal manometric measurements in terms of swallowing mechanics. *Dysphagia* **6**, 100–119 (1991).

46. Passaretti, S. *et al.* Standards for oesophageal manometry A position statement from the Gruppo Italiano di Studio Motilità Apparato Digerente (GISMAD). *Dig. Liver Dis.* **32**, 46–55 (2000).

47. Clouse, R. E. & Staiano, A. Topography of the esophageal peristaltic pressure wave. *Am. J. Physiol.-Gastrointest. Liver Physiol.* **261**, G677–G684 (1991).

48. Peirlinck, M. Design of biodegradable esophageal stents. (Universiteit Gent, Ghent, Belgium, 2013).

49. Silva, R. Esophageal Stenting: How I Do It. *GE Port. J. Gastroenterol.* **30**, 35–44 (2023).

50. Ferhatoglu, M. F. & Kıvılcım, T. Anatomy of Esophagus. in *Esophageal Abnormalities* (ed. Chai, J.) (IntechOpen, Rijeka, 2017). doi:10.5772/intechopen.69583.

51. Mittal, R. K. & Balaban, D. H. The Esophagogastric Junction. *N. Engl. J. Med.* **336**, 924–932 (1997).

52. Mowlavi, S. *et al.* In vivo observations and in vitro experiments on the oral phase of swallowing of Newtonian and shear-thinning liquids. *J. Biomech.* **49**, 3788–3795 (2016).

53. McCullough, G., Pelletier, C. & Steele, C. National Dysphagia Diet: What to Swallow? *ASHA Lead. Arch.* **8**, 16–27 (2003).

54. Stone, C.-B. Achalasia: nutrition therapy. *AGA GI Patient Center* https://patient.gastro.org/achalasia-nutrition-therapy/ (2021).

55. Li, Y. & Kong, F. Simulating human gastrointestinal motility in dynamic in vitro models. *Compr. Rev. Food Sci. Food Saf.* **21**, 3804–3833 (2022).

56. Mozafari, H. *et al.* Migration resistance of esophageal stents: The role of stent design. *Comput. Biol. Med.* **100**, 43–49 (2018).

57. Christie, K. N., Thomson, C. & Hopwood, D. A comparison of membrane enzymes of human and pig oesophagus; the pig oesophagus is a good model for studies of the gullet in man. *Histochem. J.* **27**, 231–239 (1995).

58. Durcan, C. *et al.* Experimental investigations of the human oesophagus: anisotropic properties of the embalmed muscular layer under large deformation. *Biomech. Model. Mechanobiol.* **21**, 1169–1186 (2022).

59. Yang, W., Fung, T. C., Chian, K. S. & Chong, C. K. Finite element simulation of food transport through the esophageal body. *World J. Gastroenterol. WJG* **13**, 1352–1359 (2007).

60. Yang, W., Fung, T. C., Chian, K. S. & Chong, C. K. Directional, Regional, and Layer Variations of Mechanical Properties of Esophageal Tissue and its Interpretation Using a Structure-Based Constitutive Model. *J. Biomech. Eng.* **128**, 409–418 (2005).

61. Lin, C. X. *et al.* Friction behavior between endoscopy and esophageal internal surface. *Wear* **376–377**, 272–280 (2017).

62. O'Leary, S. A., Doyle, B. J. & McGloughlin, T. M. The impact of long term freezing on the mechanical properties of porcine aortic tissue. *J. Mech. Behav. Biomed. Mater.* **37**, 165–173 (2014).

63. Caon, T. & Simões, C. M. O. Effect of Freezing and Type of Mucosa on Ex Vivo Drug Permeability Parameters. *AAPS PharmSciTech* **12**, 587–592 (2011).

64. Das, K. K. *et al.* Performance and Predictors of Migration of Partially and Fully Covered Esophageal Self-Expanding Metal Stents for Malignant Dysphagia. *Clin. Gastroenterol. Hepatol.* **19**, 2656-2663.e2 (2021).

65. Jaber, F. *et al.* A Comprehensive Analysis of Reported Adverse Events and Device Failures Associated with Esophageal Self-Expandable Metal Stents: An FDA MAUDE Database Study. *Dig. Dis. Sci.* **69**, 2765–2774 (2024).

66. Seven, G. *et al.* Partially versus fully covered self-expanding metal stents for benign and malignant esophageal conditions: a single center experience. *Surg. Endosc.* **27**, 2185–2192 (2013).

67. Hong, S. J., Bhargava, V., Jiang, Y., Denboer, D. & Mittal, R. K. A Unique Esophageal Motor Pattern That Involves Longitudinal Muscles Is Responsible for Emptying in Achalasia Esophagus. *Gastroenterology* **139**, 102–111 (2010).

68. Salvador, R. *et al.* Manometric pattern progression in esophageal achalasia in the era of high-resolution manometry. *Ann. Transl. Med.* **9**, 906–906 (2021).

69. Salvador, R. *et al.* The natural history of achalasia: Evidence of a continuum—"The evolutive pattern theory". *Dig. Liver Dis.* **50**, 342–347 (2018).

70. Blonski, W., Vela, M., Hila, A. & Castell, D. O. Normal values for manometry performed with swallows of viscous test material. *Scand. J. Gastroenterol.* **43**, 155–160 (2008).

71. Ang, D. *et al.* Diagnostic yield of high-resolution manometry with a solid test meal for clinically relevant, symptomatic oesophageal motility disorders: serial diagnostic study. *Lancet Gastroenterol. Hepatol.* **2**, 654–661 (2017).

72. Qazi, W. M., Ekberg, O., Wiklund, J., Kotze, R. & Stading, M. Assessment of the Food-Swallowing Process Using Bolus Visualisation and Manometry Simultaneously in a Device that Models Human Swallowing. *Dysphagia* **34**, 821–833 (2019).

73. Dellon, E. S. *et al.* Viscous Topical is More Effective than Nebulized Steroid Therapy for Patients with Eosinophilic Esophagitis. *Gastroenterology* **143**, 321-324.e1 (2012).

74. Steiger, C. *et al.* Ingestible electronics for diagnostics and therapy. *Nat. Rev. Mater.* **4**, 83–98 (2019).

75. Rafeedi, T. *et al.* Wearable, epidermal devices for assessment of swallowing function. *Npj Flex. Electron.* **7**, 1–19 (2023).

76. Kim, Y. *et al.* Simulator-based training method in gastrointestinal endoscopy training and currently available simulators. *Clin. Endosc.* **56**, 1–13 (2023).

77. Elisha, G. *et al.* Neurological disorders leading to mechanical dysfunction of the esophagus: an emergent behavior of a neuromechanical dynamical system. Preprint at https://doi.org/10.48550/arXiv.2402.18103 (2024).

78. Peirlinck, M. *et al.* An in silico biomechanical analysis of the stent–esophagus interaction. *Biomech. Model. Mechanobiol.* **17**, 111–131 (2018).

79. Sommer, G. *et al.* Multiaxial mechanical response and constitutive modeling of esophageal tissues: Impact on esophageal tissue engineering. *Acta Biomater.* **9**, 9379–9391 (2013).

80. Din, S., Xu, W., Cheng, L. K. & Dirven, S. A Stretchable Array of Electronic Receptors for Esophageal Swallowing Robot for Biomimetic Simulations of Bolus Transport. *IEEE Sens. J.* **18**, 5497–5506 (2018).

81. Dirven, S. *et al.* Design and Characterization of a Peristaltic Actuator Inspired by Esophageal Swallowing. *IEEEASME Trans. Mechatron.* **19**, 1234–1242 (2014).

82. Xavier, M. S., Fleming, A. J. & Yong, Y. K. Finite Element Modeling of Soft Fluidic Actuators: Overview and Recent Developments. *Adv. Intell. Syst.* **3**, 2000187 (2021).

83. Chen, J. *et al.* Determination of oral mucosal Poisson's ratio and coefficient of friction from in-vivo contact pressure measurements. *Comput. Methods Biomech. Biomed. Engin.* **19**, 357–365 (2016).

84. May, A., Nachbar, L., Schneider, M., Neumann, M. & Ell, C. Push-and-Pull Enteroscopy using the Double-Balloon Technique: Method of Assessing Depth of Insertion and Training of the Enteroscopy Technique using the Erlangen Endo-Trainer. *Endoscopy* **37**, 66–70 (2005).

85. Neumann, M. *et al.* The Erlangen Endo-Trainer: Life-Like Simulation for Diagnostic and Interventional Endoscopic Retrograde Cholangiography. *Endoscopy* **32**, 906–910 (2000).

86. Vick, L. R., Vick, K. D., Borman, K. R. & Salameh, J. R. Face, Content, and Construct Validities of Inanimate Intestinal Anastomoses Simulation. *J. Surg. Educ.* **64**, 365–368 (2007).

87. Lu, X. & Gregersen, H. Regional distribution of axial strain and circumferential residual strain in the layered rabbit oesophagus. *J. Biomech.* **34**, 225–233 (2001).

88. Karcher, A., Schäfer, J., Cattaneo, G. & Sanchez, D. Development of a measurement setup to determine the frictional properties of tissuemimicking materials for vascular models. *Curr. Dir. Biomed. Eng.* **10**, 356–359 (2024).

89. Kim, J.-S. *et al.* Experimental investigation of frictional and viscoelastic properties of intestine for microendoscope application. *Tribol. Lett.* **22**, 143–149 (2006).

90. Peng, L., Roch, T., Bonn, D. & Weber, B. The Decrease of Static Friction Coefficient with Interface Growth from Single to Multiasperity Contact. *Phys. Rev. Lett.* **134**, 176202 (2025).

91. Dionisio, P. *et al.* High Resolution Esophageal Manometry (HRM): Topographical Mapping of Esophageal Motor Function in Scleroderma: 45. *Off. J. Am. Coll. Gastroenterol. ACG* **103**, S18 (2008).

92. Dragon Skin™ 20 Product Information. *Smooth-On, Inc.* https://www.smooth-on.com/products/dragon-skin-20/.

93. Ecoflex™ 00-30 Product Information. *Smooth-On, Inc.* https://www.smooth-on.com/products/ecoflex-00-30/?quicksearch.

94. Zhang, X., Lu, Y., Li, Y., Zhang, C. & Wang, R. Numerical calculation and experimental study on response characteristics of pneumatic solenoid valves. *Meas. Control* **52**, 1382–1393 (2019).

95. Babaei, A., Bhargava, V. & Mittal, R. K. Upper esophageal sphincter during transient lower esophageal sphincter relaxation: effects of reflux content and posture. *Am. J. Physiol. - Gastrointest. Liver Physiol.* **298**, G601–G607 (2010).

96. Mittal, R. K. & Zifan, A. Why So Many Patients with Dysphagia Have Normal Esophageal Function Testing. *Gastro Hep Adv.* S2772572323001589 (2023) doi:10.1016/j.gastha.2023.08.021.

97. Paterson, W. G., Goyal, R. K. & Habib, F. I. Esophageal motility disorders. *GI Motil. Online* https://doi.org/10.1038/gimo20 (2006) doi:10.1038/gimo2

Acknowledgments

The authors thanks Gang Shen for support with frictional testing. N.A.P. gratefully acknowledges the Visiting Professor position in MIT Department of Mechanical Engineering during his academic leave from Northwestern University in Fall 2023 and Winter 2024. S.K. acknowledges Mark Fitzmaurice and Sword Medical Ltd. for the loan of equipment.

Funding

Taighde Éireann – Research Ireland grant GOIPG/2023/3917 (SK)
Taighde Éireann – Research Ireland grant 13/RC/2073_P2 (E.D.O'C.)
Karl van Tassel (1925) Career Development Professorship (GT)
Department of Mechanical Engineering, MIT (GT)
Division of Gastroenterology, Brigham and Women's Hospital (GT)

Author contributions:

Conceptualization: SK, WWC, GT, EDO'C
Methodology: SK, GT, NAP, EDO'C
Investigation: SK
Funding acquisition: SK, GT, EDO'C
Project administration: GT, EDO'C
Supervision: GT, EDO'C
Writing – original draft: SK
Writing – review & editing: SK, NAP, WWC, GT, EDO'C

Competing interests

Complete details of all relationships for profit and not for profit for G.T. can be found at the following link: https://www.dropbox.com/sh/szi7vnr4a2ajb56/AABs5N5i0q9AfT1IqIJAE-T5a?dl=0. The other authors declare that they have no competing interests.

FIGURE CAPTIONS

Fig. 1. Overview of the approach.
a, Biodesign approach through anatomical structure of esophagus, computational replication, and representation of physical replication. Direction of gravity relative to model and upright humans is shown. **b,** The model was designed computationally to replicate the three main stages of a swallowing wave and the muscle mechanics that coordinates them. These main stages are (1) the passive state of the esophagus, (2) the pre-bolus contraction stage, and (3) the post-bolus relaxation stage. **c,** The three studies that were conducted with the model to demonstrate its versatility were evaluation of stent migration and the effect of bolus viscosity on achalasia diagnosis and dietary recommendations. **d,** A visual comparison between the passive (upper images) and contracted (lower images) states in a human esophagus and in the proposed soft-robotic esophagus. Human images reprinted from *The Current Main Types of Capsule Endoscopy* in *Handbook of Capsule Endoscopy*, Li *et al.*, Springer Netherlands, 2014, reproduced with permission from Springer Nature.

Fig. 2. Computational design.
a, Comparison of lumen shape at passive stage for models with circular, triangular, square, pentagonal, and hexagonal shaped rings against that of porcine oesophageal tissue. **b,** Dice-Sørensen similarity coefficient (DSC**)** for each of the shapes in A. **c,** Turning distance for each of the shapes in A. **d,** Independence study when actuating longitudinal and circumferential chambers separately, with insets of FEA models illustrating deformation of the chambers under pressurized cycle compared to original geometry (white). White and red X's denote original and current location of point being tracked for displacement, with white line denoting the point's path between X's. Top graph: Input pressures applied to circumferential and longitudinal chambers as a percentage of their peak pressure over time. Middle graph: Corresponding radial and axial displacement of the point for the EcoFlex 00-30 only model. Bottom graph: Corresponding radial and axial displacement of the point for EcoFlex 00-30 and DragonSkin 20 model. **e-f,** The correlation coefficient was calculated between the top graph and **(e)** axial displacement post-decoupling in the middle graph (correlation coefficient = 0.64) and **(f)** axial displacement post-decoupling in the bottom graph (correlation coefficient = 0.98). Porcine tissue image in **b** is reprinted from *Journal of Biomechanics*, Vol. 40, Yang *et al.*, *Instability of the two-layered thick-walled esophageal model under the external pressure and circular outer boundary condition*, pp. 481-490, Copyright (2007), with permission from Elsevier.

Fig. 3. Computational and experimental characterization of model.
a-b, High resolution manometry testing of model simulating swallowing wave carried out **(a)** computationally and repeated (**b)** experimentally (image mirrored for clarity). **c,** A comparison of the resulting HRM topography plots for both computational (upper) and experimental (lower) tests. Black line running along HRM topography plots shows timepoints along which each corresponding pressure vs time plot taken from. HRM image (left) adapted with permission from Esophageal manometry test, A.D.A.M. Medical Illustration © 2026.

Fig. 4. Comparison of commercial stent's migration in soft-robotic model.
a, High-resolution topography map showing input wave using PIV loop and wave repeated using recorded PWM values for consistency. **b,** Commercial stents used for study. **c-d,** Measured displacements of stents over 30 swallow cycles (n = 5) in **(c)** benchtop model without esophageal tissue and **(d)** benchtop model with esophageal tissue. **e-f,** Images of stents at initial swallow cycle (left) and final swallow cycle (right) in **(e)** model without tissue and **(f)** model with tissue. **g,** A regression model for RoboGullet showing the estimated change in displacement when, if all other parameters are held constant, brand is changed from A to B, or type is changed from fully-covered to partially-covered, or OD is increased by 1mm. **h,** Comparison in displacements between the FC Stent III and the PC Stent V, both of Brand B, when the model had tissue added to it versus when it did not. **i,** Measured displacement of Stent A with isolated and combined circumferential longitudinal muscle movement. Bar and line plots show mean and standard deviations; * $P < 0.05$, ** $P < 0.01$.

Fig. 5. Simulation of normal and achalasia swallows within Chicago Classification clinical metrics and effect of bolus viscosity on these metrics.
a, High resolution manometry topography plots of normal and achalasia type III, type II, and type I swallows simulated with soft-robotic model with the clinical metrics for achalasia labelled. Distal Contractile Integral (DCI) = wave amplitude × duration × length of the distal esophageal contraction exceeding 20 mmHg from the transition zone to the proximal margin of the LES [11]. Integrated Relaxation Pressure (IRP) = mean of the pressure at the

esophagogastric junction (distal end of LES) over the 4 second window of maximal relaxation beginning after UES relaxation [11]. Distal Latency (DL) = interval in seconds between UES relaxation and contraction of point ~3cm above proximal part of LES [11]. **b-d,** Plots of the measured clinical metrics **(b)** Distal latency (DL), **(c)** distal contractile index (DCI), and **(d)** integrated relaxation pressure for normal and motility disease states for n = 3 swallows with grey overlay of Chicago Classification threshold range for each state. **e-i,** Effect of bolus viscosity on **(e)** DL for normal swallow, **(f)** DL and **(g)** IRP for achalasia type III, **(h)** IRP for achalasia type II, and **(i)** IRP for achalasia type I (n = 3). **j,** Weight of bolus that traversed the soft-robotic esophagus after 5 minutes for achalasia type II (left) and achalasia type I (right) (n = 5). Bolus used was 5mL of refrigerated Greek yoghurt that was left unstirred (US) or stirred (S) before swallowing. Box plot indicates the minima, maxima, and median, first and third quartile, with individual measurements as dots. Bar and line plots show mean and standard deviations; * $P < 0.05$. Sample sizes: motility metrics (b-i) n = 3, yoghurt motility (j) n = 5.

Editor's Summary
Esophageal motility is difficult to model accurately, hindering studies of dysphagia and achalasia. The authors present a soft-robotic esophagus that independently replicates muscle actions to simulate both healthy and diseased swallowing.

Peer review information: *Nature Communications* thanks the anonymous reviewer(s) for their contribution to the peer review of this work. A peer review file is available.

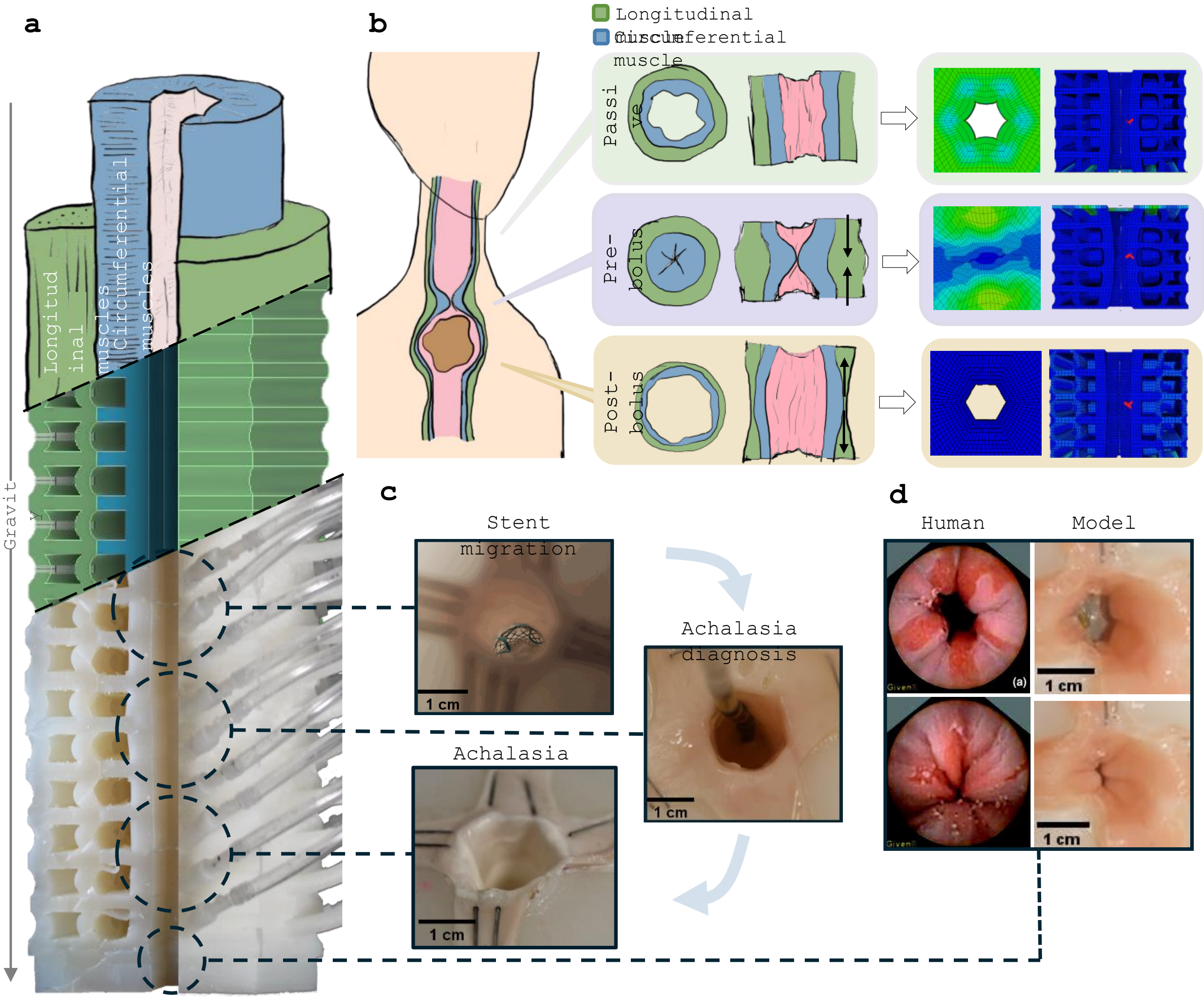
a
b
Longitudinal muscle
Circumferential muscle
Longitud inal muscles
Circumferential muscles
Gravit
Passi ve
Pre-bolus
Post-bolus
c
Stent migration
1 cm
Achalasia diagnosis
1 cm
Achalasia
1 cm
d
Human
Model
(a)
1 cm
1 cm

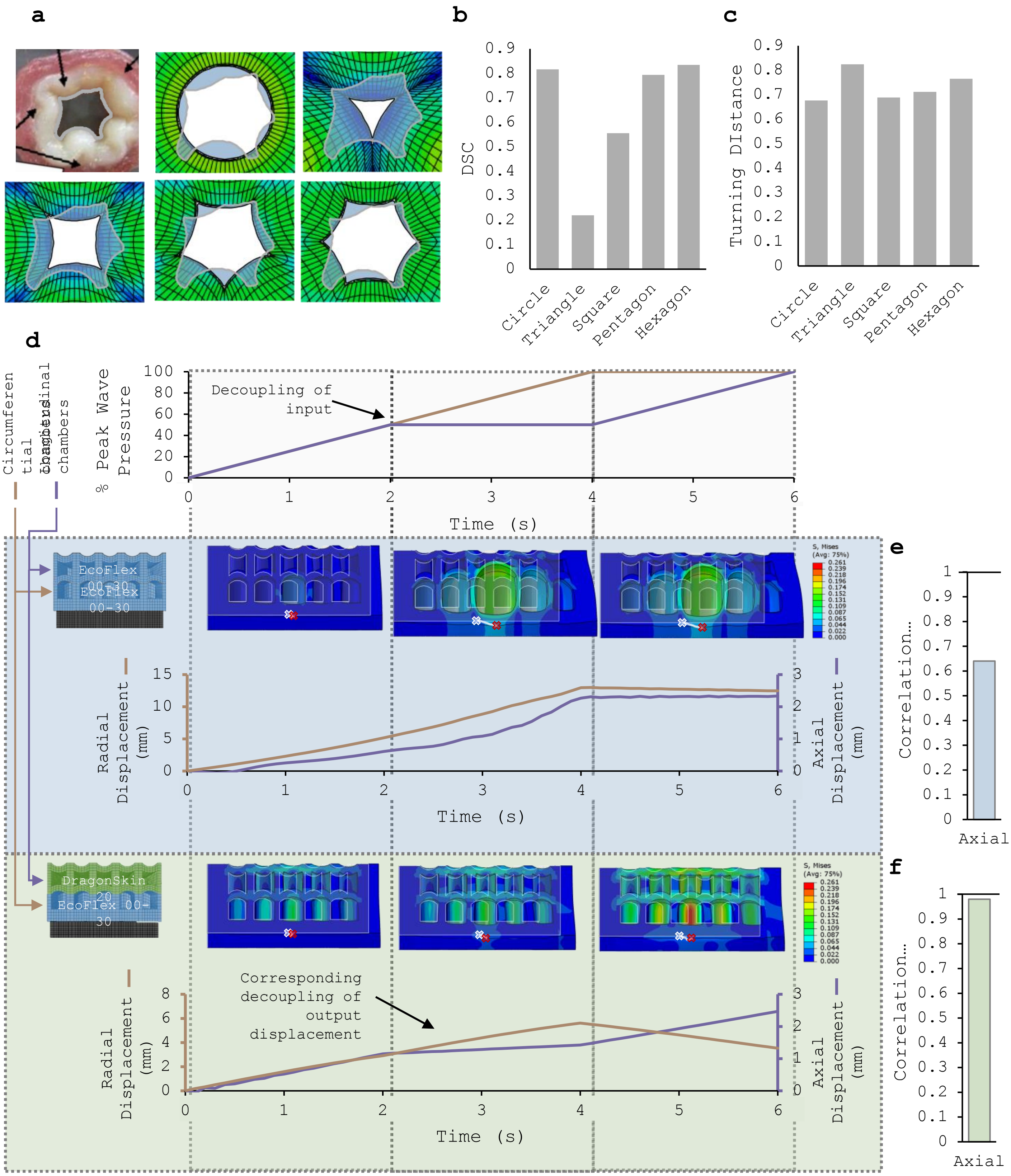
a
b
DSC
Circle
Triangle
Square
Pentagon
Hexagon
c
Turning DIstance
d
Circumferential chambers
Longitudinal chambers
% Peak Wave Pressure
Decoupling of input
Time (s)
EcoFlex 00-30
EcoFlex 00-30
Radial Displacement (mm)
Axial Displacement (mm)
e
Correlation...
Axial
DragonSkin 20
EcoFlex 00-30
Corresponding decoupling of output displacement
f
S, Mises (Avg: 75%)

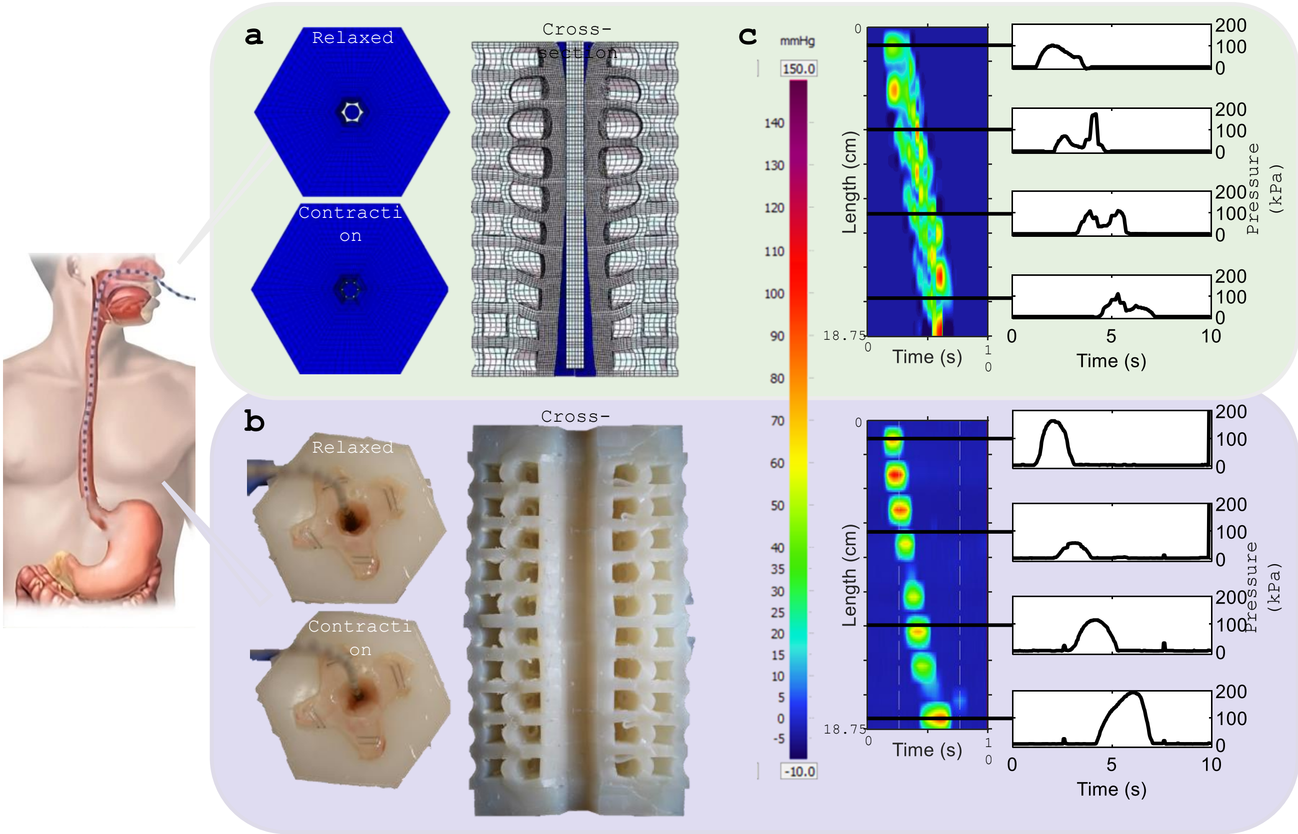

a
Relaxed
Contraction
Cross-section
b
Relaxed
Contraction
Cross-
c
mmHg
150.0
-10.0
Length (cm)
Time (s)
18.75
Pressure (kPa)
200
100
0
0
5
10
Time (s)

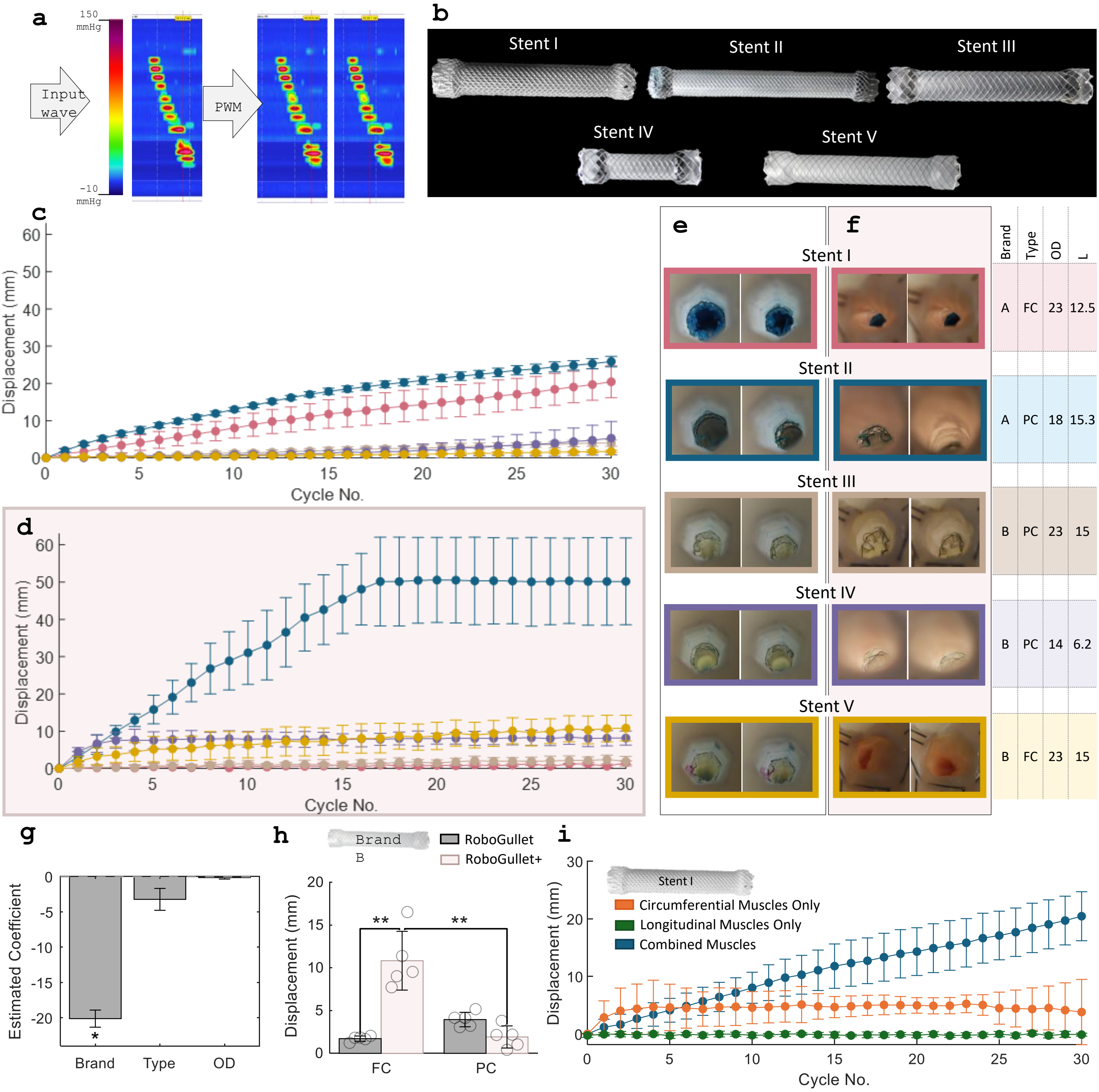
a
150 mmHg
-10 mmHg
Input wave
PWM
b
Stent I
Stent II
Stent III
Stent IV
Stent V
c
Displacement (mm)
Cycle No.
d
Displacement (mm)
Cycle No.
e
f
Stent I
Stent II
Stent III
Stent IV
Stent V
Brand
Type
OD
L
A FC 23 12.5
A PC 18 15.3
B PC 23 15
B PC 14 6.2
B FC 23 15
g
Estimated Coefficient
Brand
Type
OD
h
Brand B
RoboGullet
RoboGullet+
Displacement (mm)
FC
PC
i
Stent I
Circumferential Muscles Only
Longitudinal Muscles Only
Combined Muscles
Displacement (mm)
Cycle No.

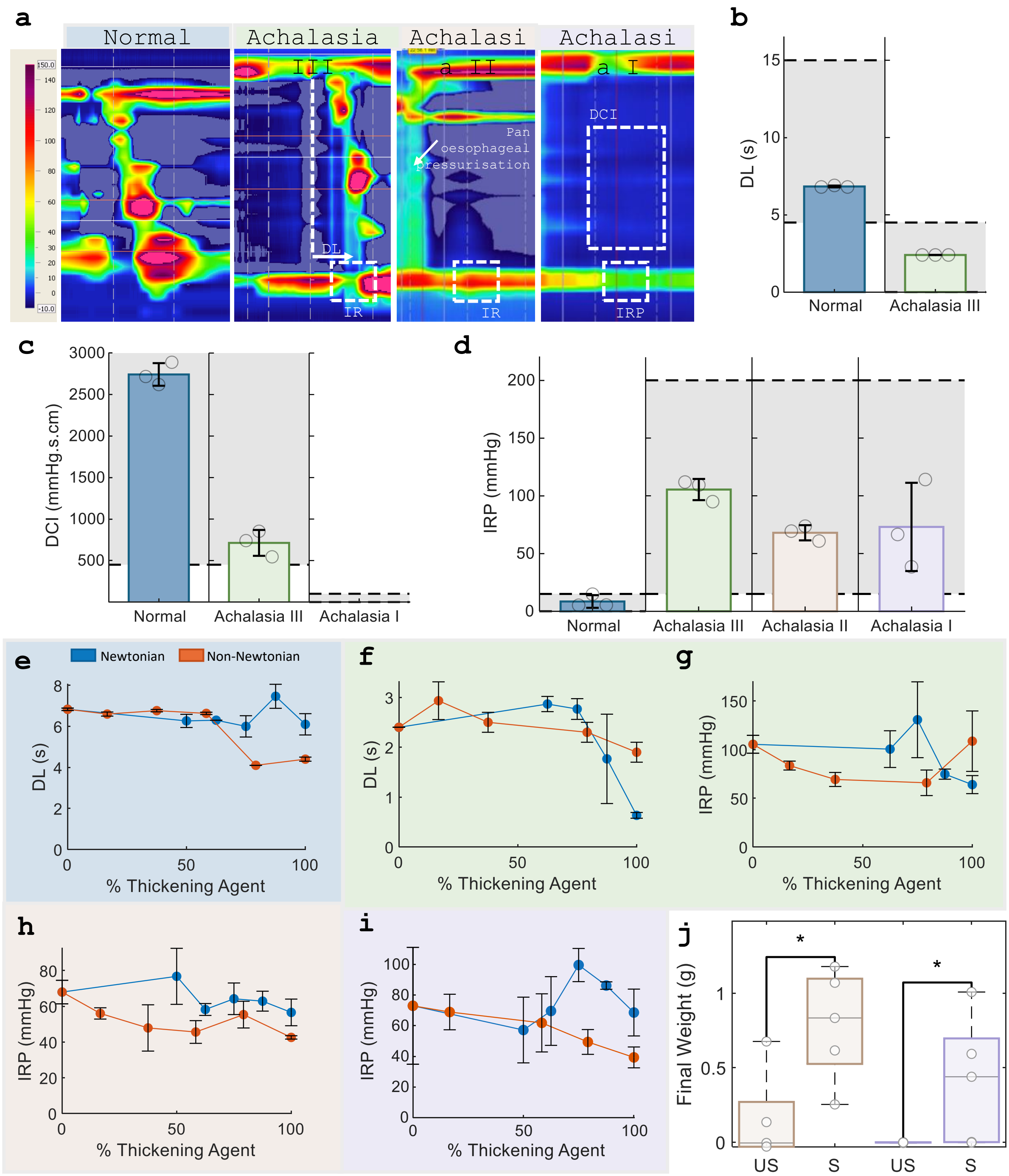
a
Normal
Achalasia III
Achalasia II
Achalasia I
DL
IR
Pan oesophageal pressurisation
DCI
IRP
b
DL (s)
Normal
Achalasia III
c
DCI (mmHg.s.cm)
Normal
Achalasia III
Achalasia I
d
IRP (mmHg)
Normal
Achalasia III
Achalasia II
Achalasia I
e
Newtonian
Non-Newtonian
DL (s)
% Thickening Agent
f
DL (s)
% Thickening Agent
g
IRP (mmHg)
% Thickening Agent
h
IRP (mmHg)
% Thickening Agent
i
IRP (mmHg)
% Thickening Agent
j
Final Weight (g)
US
S
US
S